

# **An Automated System for the Analysis of Gravity Waves and Other Mesoscale Phenomena**

STEVEN E. KOCH\*

*NOAA Research — Forecast Systems Laboratory Boulder, Colorado*

STEPHEN SALEEBY

*Colorado State University Ft. Collins, Colorado*

Revised for publication in Weather and Forecasting July 12, 2001

## **Abstract**

An automated near-real-time system for the surface analysis of gravity waves and other mesoscale phenomena is developed, tested, and applied to several cases. Five-minute observations from the Automated Surface Observing System (ASOS) network provide the primary source of data for the mesoanalysis system. ASOS time-series data are downloaded, subjected to considerable quality control, bandpass filtered and objectively analyzed using a time-to-space conversion (TSC) adaptation of the traditional Barnes scheme. The resultant analyses, which can resolve features in the ASOS network with wavelengths as short as 150 km and at 15-min intervals, are made available as animated contoured fields.

Even though this mesoanalysis system was designed primarily for gravity wave detection, it is capable of resolving other kinds of mesoscale phenomena and allowing the analyst to monitor their changing structure. The effectiveness of the system is demonstrated with two recent events selected from several cases that have been analyzed. The first case consisted of a gravity wave train that propagated through the Ohio River Valley and produced multiple precipitation bands. The second event involved a complex family of mesohighs and wake-lows associated with a convective system over the southeastern United States. Variations in the surface wind field and precipitation distribution are related to the mesoscale pressure field in both cases.

The ability of this mesoanalysis system to monitor mesoscale phenomena resides in the successful application of TSC principles to high temporal resolution surface data. Although the TSC assumption may not be strictly valid in more complex situations, for many applications this mesoanalysis system offers critical information needed for making accurate nowcasts, with the caveat that the means by which ASOS 5-min data are made available can be improved.

---

*Corresponding author address:* Dr. Steven E. Koch, NOAA Forecast Systems Laboratory, R/FS1, 325 Broadway, Boulder, CO 80305-3328. e-mail: koch@fsl.noaa.gov

## 1. Introduction

The various systems comprising the National Weather Service (NWS) modernization (Friday 1993) have now been fully implemented: the Weather Surveillance Radar (WSR-88D) network, the NOAA Profiler Network, the Automated Surface Observing System (ASOS), and the Geostationary Operational Environmental Satellite (GOES-Next). Among these systems, the one that has undeniably had the least positive impact so far upon the ability of forecasters to detect and analyze mesoscale weather phenomena is ASOS. It would seem to some that ASOS has merely replaced a manual observing procedure with an automated one, although additional benefits have been realized from the introduction of new instrumentation systems in ASOS. This lack of significant impact is most regrettable, since two aspects of ASOS have not been well exploited for mesoscale observing purposes — the availability of digital rather than analog data and 5-min rather than hourly data. The present study demonstrates that these two attributes together provide the basis for conducting national mesoanalyses operationally.

The original motivation for developing this automated mesoanalysis system was the desire to be able to detect and analyze gravity waves in real time. Case studies have established that mesoscale gravity waves (wavelengths of 50–500 km) can produce bands of heavy precipitation and severe local weather resulting from the wave-induced rising and sinking motions, as discussed in the reviews by Uccellini and Koch (1987), hereafter UK87, and Koch and O’Handley (1997), hereafter KOH97. An in-phase relationship between the pressure and winds produces the strongest updraft (downdraft) 1/4 wavelength ahead of the wave ridge (trough) according to the Eom (1975) wave conceptual model ([Fig. 1a](#)). Actually, precipitation bands typically form between

the wave ridge and the updraft due to a time lag between the onset of vertical motions and cloud formation.

Despite the significant impact that gravity waves can impose upon weather conditions and their common occurrence, these phenomena are rarely considered in preparation of NWS forecast discussions. The forecaster is largely concerned with meteorological phenomena that are better understood and more easily detected and examined through satellite and radar imagery and numerical model results. For these reasons, gravity waves have remained primarily of research interest and have yet to find their way into daily operational forecasting practices.

Nevertheless, evidence continues to mount that mesoscale gravity waves occur in an easily identifiable synoptic environment. This would indicate that the occurrence of these phenomena (their general location and timing) can be forecast with some skill, although the details of the waves and their precise effects upon the sensible weather cannot yet be predicted deterministically. This synoptic pattern, as identified by UK87 and further refined by KOH97, consists of a negatively tilted, highly diffluent trough in the 300-hPa geopotential height field, and a dynamically unbalanced jet streak that is advancing toward the axis of inflection in the height field. These studies showed that the gravity waves typically first appear near the inflection axis and north of a warm or stationary front at the surface (thus, the lower troposphere is markedly stable). The waves then propagate downstream from the inflection axis toward the upper-level ridge axis. A schematic depiction of the UK87 conceptual model is shown in [Fig. 1b](#).

Koch and Siedlarz (1999) detected coherent, long-lasting waves in the mean sea level pressure field with amplitudes of at least 0.2 hPa in the central United States 32% of the time during a 6-week period in which a large mesoscale observing network was in

place. They applied the technique of time-to-space conversion (TSC) to the microbarograph data to permit tracking of disturbances with wavelengths  $\lambda$  as small as only twice the average station spacing ( $\lambda \sim 150$  km). They also found that the largest amplitude events occurred in a UK87 type of environment.

Koppel et al. (2000) compiled a 25-yr climatology of “gravity wave events” with amplitudes of at least 4.25 hPa. They calculated an average of 23 such large-amplitude events per year, with the greatest occurrence in cyclonic storm situations peaking between the months of November and April, and those associated with convection peaking in the summer months. The two regions most impacted from waves associated with cyclones were the Midwestern United States and the area extending northward from Virginia along the eastern seaboard. The gravity waves in these two regions were consistently generated in an environment described by the UK87 model, just as was found for the central United States by Koch and Siedlarz (1999).

It thus appears that *mesoscale* gravity waves preferentially occur in a manner consistent with the UK87 conceptual model (although not necessarily generated by unbalanced flow). For this reason, and the fact that gravity wave analysis was the original motivation for designing the mesoanalysis system described here, this conceptual model was invoked in deciding when to activate the system. KOH97 proposed that mesoscale gravity waves could not only be anticipated using the UK87 conceptual model, but that they could also be detected and analyzed in near real-time because of the NWS modernization. Given the ability to perform a mesoscale analysis in real-time, a forecaster could readily examine convective systems and the evolving relationship between these systems and the associated perturbation fields. With color animated displays of radar reflectivity and

mesoanalyses of surface wind and pressure perturbations, a forecaster is well equipped to make an educated judgment as to the intensity and lifetime of such systems. Given the diagnosed presence of a gravity wave event and a region of strong wave ducting (the ability of the atmosphere to trap waves and limit wave dispersion and dissipation), it should be possible to issue a short-range forecast suggesting the possibility that bands of convection would form transverse to the mid-level flow for however long the downstream ducting potential remains strong and the forcing for the associated convection persists. Knowledge that significant gravity waves are present also could be quite useful for nowcasting damaging winds. For a pure gravity wave, the associated winds can be forecast with the use of the wave impedance relation (Gossard and Hooke 1975), which is given as  $\Delta u = -\Delta p / \rho C$ , where  $\Delta u$  is the wave-normal wind perturbation,  $\Delta p$  is the pressure perturbation,  $\rho$  is the density, and  $C$  is the ground-relative wave phase speed. For example, given a 3 hPa pressure change and a phase speed of  $20 \text{ m s}^{-1}$ , the wave-normal wind would be  $15 \text{ m s}^{-1}$ .

This paper reports on the development, testing, and application of the mesoanalysis system first proposed by KOH97. A multi-step process that utilizes 5-min ASOS data forms the basis of the system (Fig. 1c). The data are analyzed within designated sub-regions located over the eastern two-thirds of the United States following considerable quality control, bandpass filtering, and a TSC-modified Barnes objective analysis procedure (Barnes 1973; Koch et al. 1983). Mapped perturbation fields of pressure and wave-normal wind component, as well as more conventional fields, are created and then transferred to an Internet web site (<http://hugo.atmos.colostate.edu/www/gwave.html>) where the analyses are made available for researchers and operational forecasters alike. Since gravity waves are easier to detect

from animating color-contoured fields, this feature is included. Thus far, product fields have been made available in a few hours after real-time as a demonstration of the concept for real-time operational purposes (changes needed to achieve actual real-time capability are discussed in section 5).

Details of the automated mesoanalysis system, including the results of a rigorous series of analysis sensitivity tests, are discussed. Two of the meteorological events that have been analyzed by this pseudo-real-time system during the first two years (1999–2000) of system activation are also presented. Examination of the phenomena that were captured by this mesoanalysis system has shown that the technique is not limited to the analysis of gravity waves. Other features with similar mesoscale spatial and temporal scales can be distinguished, including convective mesohighs and wake-lows, gust fronts, and frontal deformation zones<sup>1</sup>. This paper demonstrates the ability of the mesoanalysis system to detect several of these phenomena.

## 2. Automated detection of mesoscale phenomena

### a. *Restricted access to the real-time ASOS data*

This mesoanalysis system was developed while both authors were at North Carolina State University to demonstrate that gravity waves could be analyzed in pseudo-real-time using only operationally available data. The system developed for this purpose involves a complex series of steps, in which the ASOS high-resolution data are first reformatted and parsed, and then processed through a series of quality control, bandpass filter, and objective

analysis programs. The final product is a collection of animated, color-contoured fields of pressure perturbations, wave-normal wind perturbations, temperature, observed winds, and altimeter pressure that are made available via on the Internet.

North Carolina State University was granted limited access to the 5-min ASOS data by the NWS Observing Systems Branch in November 1998. Access was restricted to three specified time slots per day, each of ~3-h duration. Multiple analysis subregions were created to handle the restrictions imposed by this limited access time window and the 2.0–2.5h needed to download ~10 h of the most current data from 75–80 stations by modem at the rate of 2 min per station. Because of these constraints, the subregions had to overlap in order to achieve continuity in the objective analyses. The entire station array, three of the nine subregions created to acquire and process the data, and the grid domains for the surface objective analyses in each of these subregions are shown in [Fig. 2](#). The lengthy download time of ~2 h, the additional loss of ~2 h of data on both ends of the time series due to temporal bandpass filtering, and the 30-min computer processing time, meant that each set of analyses could only be made available ~4.5 h after real time. The needed modifications to this prototype system to make it fully real-time are discussed later.

### b. *Deciding when to activate the mesoanalysis system*

The original impetus for the development of this mesoanalysis system stems from the work of KOH97, in which a viable methodology for the real-time prediction and analysis of mesoscale gravity waves was first articulated. They envisioned such a system to potentially serve as a proof-of-concept for use in an NWS forecast office in the near future. At the current time, the high telecommunications costs entailed in running an analysis system that uses a modem to

---

<sup>1</sup> For a demonstration of how a spatial bandpass filter can be applied to mesoscale model fields to isolate frontal deformation and surface convergence zones, see Koch et al. (1998).

access ASOS data, and the fact that weather-producing gravity waves are not an everyday occurrence, means that it is not practical to run the system on a continual basis. In fact, KOH97 suggested that the automated analysis system should only be activated when the synoptic flow is favorable for gravity wave occurrence according to the UK87 model, and further diagnostic analysis of mesoscale model forecast fields reveals the presence of upper-level unbalanced flow and low-level wave ducting.

Although it was discovered *ex post facto* that other mesoscale phenomena besides gravity waves could be analyzed by this prototype system (e.g., as demonstrated in section 4b), the procedure used for deciding when to activate the system consisted of the 5-step process advocated by KOH97 for gravity wave analysis:

- 1) Determine whether the UK87 conditions favorable for gravity waves are present.
- 2) Compute unbalanced flow indicator fields and wave ducting potential (described below) to further delineate the gravity wave threat area.
- 3) Activate an automated gravity wave detection system using bandpass-filtered 5-min data from the ASOS network.
- 4) Determine whether the resulting surface mesoanalysis shows evidence of gravity waves by examining whether the perturbation pressure and wind fields behave in a manner consistent with the impedance relationship from gravity wave theory.
- 5) Modify the short-term forecast to include consideration of gravity wave influences upon precipitation and clouds, including the possibility in some cases of hazardous winter weather or severe thunderstorms.

Upon finding a favorable wave environment according to the UK87 conceptual model, diagnostic model analyses were used to determine the degree of

unbalanced flow in proximity to an upper-level jet streak and the possible existence and strength of a wave duct at low levels. The concepts of “unbalanced flow” and “wave ducting potential” deserve further explanation. KOH97 and Zhang and Koch (2000) discuss the merits of the residual of the nonlinear balance equation as an indicator of unbalanced flow. The nonlinear balance equation involves four terms representing a balance between the synoptic scale rotational wind component and the geopotential field. In the gravity wave environment of the UK87 model, the terms for the Laplacian of geopotential and the Jacobian of the winds typically are dominant and of the same sign. This results in large non-zero values of the equation, which indicates imbalance and large parcel divergence tendency in the diffluent jet exit region downstream from the base of a trough.

If unbalanced flow was indicated in the model forecast fields, then the environment downstream from this potential wave generation region was examined to see if an efficient duct for preventing loss of wave energy was present. The ducting theory of Lindzen and Tung (1976), simplified according to the “wave duct factor” method advocated by KOH97, was applied for this purpose. The wave duct factor is a measure of the strength of the low-level stratification and the degree to which the 400-700 hPa layer is conditionally unstable, which together are required for a wave duct sufficient to impede the vertical leakage of wave energy. Values of the duct factor larger than ~10-15 are significant enough to represent regions of strong ducting. Forecast soundings and vertical cross sections near the anticipated wave corridor were also examined for the presence of the correct thermodynamic structure, and whether the layer of conditional instability contained a wave “critical level” (in which the wave phase speed equals the wind speed component in the direction of wave propagation). These conditions are

needed for a strong wave duct. Scripts were written to automate the calculation of these diagnostics on a variety of mesoscale numerical weather prediction models available to this project.

The measures described above were taken to further refine the region for downloading ASOS data for gravity wave analysis. If all of the above conditions (the UK87 pattern, diagnosed imbalance, and a strong wave duct) were met over some region in the model forecast fields, the decision was made to download ASOS data and initiate a series of data manipulation processes over that region. Although this procedure was used in deciding whether to activate the system during its prototype development stage, real-time mesoanalysis may be performed for many other non-gravity wave applications with one minor change (discussed in section 3a).

#### *c. Quality control of ASOS 5-min data*

The multi-step process of data retrieval and processing by which the mesoanalyses are obtained ([Fig. 1c](#)) begins with the extraction of meteorological parameters of interest from the downloaded ASOS datastream. Quality control (QC) is then conducted upon these data to attempt to detect and eliminate potentially erroneous data embedded within the time series. The quality control system is composed of a sequence of routines followed by selective application of an interpolator to fill in small-scale data gaps left by the QC and to reduce discontinuities.

The first QC routine searches for time discontinuities in the data stream and inserts any missing times. Parameters at missing times are given null values, as they are necessary placeholders for preserving time continuity. The second QC check is for tolerable and realistic ranges acceptable for each parameter. Any data point outside of the established boundaries is given a null value. The third check sets an upper limit on the magnitude of allowable 5- and 10-min

changes and eliminates any datum that exceeds the established limits. The fourth QC check searches for short-duration, small-amplitude “blips” in the data curve, i.e., a short-term spike in the time series that jumps to a different value and returns back to precisely the previous state value. Each blip point is given the value of the surrounding two data points, but blips longer than 10 min are assumed to be potentially real anomalies and are left unaltered. The fifth QC test searches for local maxima and minima in the time series data. Laplacian values exceeding a set limit are assumed to represent unrealistic changes over short time periods. Upon completion of these QC routines, a cubic Lagrangian interpolator is then implemented to fill in small gaps of up to 10 min to minimize loss of time continuity following the above data processing.

#### *d. Bandpass filtering*

The next step in the system involves bandpass filtering of the altimeter pressure and Cartesian wind component time-series data in order to produce mesoscale perturbations of pressure  $p'$  and wave-normal wind  $u'^*$ , thus enabling gravity waves to be isolated and tracked. The chosen bandpass filter is one designed by Lanczos (1956). The conflicting purposes of minimizing data loss (a consequence of filtering) and attempting to recover the full amplitude of mesoscale waves imply a highly constrained combination of variables. Wave frequencies of  $0.0037 - 0.0313 \text{ min}^{-1}$  were selected to retain and isolate mesoscale gravity waves with periods of 32 - 270 min. The corresponding filter response curve is shown in [Fig. 3](#). The requirement to minimize data loss while not sacrificing loss in wave amplitude in this frequency range resulted in the choice of  $N=49$  weights. Thus,  $(N-1)/2 = 120$  min of data was lost at each end of the time series, while obtaining a response of at least 0.50 for waves

within the entire chosen band, and excellent response of  $1.0 \pm 0.045$  for waves with periods of 36–150 min.

*e. Objective analysis*

The bandpass filtered pressure and wave-normal wind data from the network of ASOS stations are gridded using an objective analysis procedure for viewing the pressure and wind perturbations as mapped surface fields. The ASOS download region (Fig. 2) determines each grid analysis region. The gridded analyses are produced by implementation of a TSC adaptation of the Barnes (1964) objective analysis scheme, as first proposed by Barnes (1973).

The traditional Barnes (1964) scheme uses inverse Gaussian weights whose values are dependent upon the distance between the grid point and the surrounding data points within a circular search radius about each grid point. Koch et al. (1983) discuss the mathematical details and the advantages and limitations of the two-pass Barnes scheme. This traditional Barnes scheme fails to reveal wave coherence and the full wave structure at scales smaller than approximately six times the average station spacing ( $6\Delta n$ ), especially for the non-uniform ASOS station array considered here.

A TSC procedure is added to the original Barnes objective analysis method to overcome the  $6\Delta n$  limitation and even resolve waves as small as  $2\Delta n$  with near-unity response (this is proven by KOH97). The TSC-Barnes scheme acts to create new “off-time” observation points, located between stations, by transforming high-resolution time series data into spatial data according to  $\Delta \vec{X} = \vec{C} (n\Delta t)$  in which  $\vec{C}$  is the advection vector velocity and  $n\Delta t = \pm 5 \text{ min}, 10 \text{ min}, \dots, \left(\frac{N-1}{2}\right) \Delta t$ .

Thus, TSC helps fill in the gaps between data stations and grid points. This point was first

made many years ago by Fujita (1963), who combined subjective TSC mesoanalyses with radar data to gain understanding of the nature of mesoscale convection. Koch and McCarthy (1982) were the first to use an *objective* TSC technique in studying the mesoscale environment of a dryline and associated severe thunderstorms.

A visualization of the weighting function, the logic supporting the advection of off-time observations, and an example of the TSC effect for one of the real-time cases revealing the resulting extension of the area of influence between the stations are shown in Fig. 4. The off-time observations are given reduced weights (using an inverse Gaussian temporal weighting) to distinguish the TSC-Barnes scheme from time compositing techniques. The TSC objective analysis can reveal the presence and maintain the coherence of waves at scales approaching  $2\Delta n$  ( $\sim 150\text{-km}$  wavelengths for the subregions displayed in Fig. 2), provided that the advection vectors can be accurately determined *a priori*, and that horizontal advection dominates over nonconservative processes.

*f. TSC advection vector calculation*

Prior to calculating the wave-normal winds and performing the TSC Barnes objective analysis, an advection vector set equal to the horizontal wave propagation vector must be assigned to each data station. These vectors are used to calculate the wind in the direction of wave propagation and also the direction and spacing  $\Delta \vec{X} = \vec{C} (n\Delta t)$  with which off-time observations are advected in the objective analysis. KOH97 demonstrated that for mesoscale gravity waves, a mass-weighted mean wind vector in the conditionally unstable layer that overlies the stably stratified duct layer is an accurate predictor of the wave propagation vector. The wave-normal wind calculations and TSC process can only be performed in real-time

through use of such an *a priori* estimate of the wave motion vectors. For this purpose, KOH97 further showed that the 700–400 hPa layer could be used to approximate the conditionally unstable layer. The advection vectors are determined within this layer using either sounding data or model forecast fields, whichever is judged to be most representative at a given ASOS location and time.

### 3. Barnes scheme parameter testing

To achieve the desired response given the available network and the goal of isolating mesoscale features on the order of 150–300 km, a series of tests was performed to determine the most appropriate values for the various controlling parameters in the TSC-Barnes scheme. Only a subset of these test results is described here to demonstrate the difference in results obtained using the TSC-Barnes scheme instead of the conventional Barnes scheme. Tests of variations in the Barnes spatial and temporal weighting functions, the numerical convergence parameter, the length of the TSC interval ( $\tau$ ) and other factors affecting the resulting analyses are reported by KOH97.

#### *a. Comparisons between TSC-Barnes and traditional Barnes analyses*

Meaningful time-to-space conversion requires the chosen advection vector(s) to be representative of the propagation of the system(s) throughout the given region. The vector mean wind in the midtropospheric layer described above, while shown by KOH97 to be optimal for estimating gravity wave propagation, is less than ideal for many other kinds of mesoscale phenomena. For example, if the feature of interest in the mesoanalysis is a surface cold front, then the frontal motion should be used for the TSC advection vector(s). In more complex situations involving a combination of frontal

motions of various kinds, gravity waves, convective systems with their associated gust fronts, and various other convergence boundaries, it is considerably more difficult to define a set of advection vectors for use with TSC.

Whatever the case may be, the objective is to be able to define an advection vector for every ASOS surface station at each time. When use is made of sounding data for this purpose, the field of advection vectors is objectively analyzed using a conventional Barnes scheme to produce a grid-point array of vectors. Otherwise, model forecast gridpoint data might be used for assigning advection vectors to each ASOS station location.

We performed sensitivity tests in which the number of advection vectors was varied. Within a given region there could be numerous sounding sites, thereby providing an array of advection vectors in the analysis area. Tests were performed to assess the quality of the analyses given the use of different numbers of vectors that represent the flow of the mean wind in different sectors of the analysis domain. A comparison of objectively analyzed pressure perturbation fields reveals that the 0-vector analysis, which digresses to the traditional Barnes scheme, produces isolated circular perturbations with poor space-time continuity ([right panels in Fig. 5](#)). Use of a single advection vector greatly improves the space-time coherence of perturbation features. The use of multiple vectors produces realistic (arc-shaped) wave structures while removing the artificial assumption that all features in the domain are propagating with exactly the same velocity ([left panels in Fig. 5](#)).

The tremendous advantage of the TSC Barnes objective analysis over the traditional Barnes analysis lies in the simple fact that 2 – 4  $\Delta n$  wave coherence and structure are better resolved after interpolating the off-time observations into spatial data. This

comparison between the TSC analysis (using 4 advection vectors and  $\tau = 50$  min) and the traditional analysis (Fig. 5) provides demonstration of these benefits of TSC to better resolve mesoscale features and maintain them in a coherent fashion as they propagate through the analysis region.

*b. Spatial cross-covariance and temporal correlation measures*

A series of statistical calculations was performed to numerically assess the relative quality of the traditional Barnes and TSC Barnes analysis schemes. The comparisons included computations of these quantities:

- the cross-covariance between the analyzed perturbation pressure and wave-normal wind fields ( $p'u^*$  should be very high for gravity waves)
- the sequential time correlation
- the time-lagged correlation of selected pressure perturbation fields.

Representative results of the latter two sets of calculations follow, whereas the first of these comparisons is presented later in the discussion of Event 1 (section 4a).

Correlation coefficients were computed between successive 5-min grid times for a sample period of 0100–0400 UTC 14 March 1999. The sequential correlation method correlates pressure perturbation fields from one time to the subsequent time, such that the analysis at  $t_0$  is correlated to that at  $t_1$ ,  $t_1$  to  $t_2$ ,  $t_2$  to  $t_3$ , and so forth. The results (Fig. 6) show that the traditional Barnes scheme is characterized by extreme fluctuations in correlation values between successive times, thereby indicating inconsistencies and unrealistic changes in the pressure perturbation analyses between the 5-min data grids. In contrast, the TSC correlation values remain very high with only minor fluctuations over time.

A more comprehensive method of determining which objective analysis technique produces the better (more coherent) results is through a time-lagged correlation analysis. This method compares the gridded analysis of pressure perturbations at an initial time to the continuously time lagged grids, such that the analysis at  $t_0$  is correlated to that at  $t_1$ , then to  $t_2$ , and so forth to the end of the time sample. A displacement vector at each grid point was used to search within a given radius for the grid point that maximizes the correlation value at a given time. Displacement vectors effectively track features as they propagate by continually relating grid patterns at one time and place to the correlated “downstream” ones. Each grid point was allowed a finite radius of influence to search for the best local correlation, with the radius limit constrained by the conceivable distance a feature could propagate within the given time lag. After calculating aggregate correlations for each allowed radius, the domain correlation coefficients were calculated for each vector and the largest coefficient was retained for the final analysis.

This process was repeated for each 5-min time lag and for both the TSC and traditional Barnes analyses of pressure perturbation. A graph of the time-lagged correlation values for the two schemes reveals that TSC values drop off much more slowly with increasing time lag, thereby revealing a more coherent and realistic data analysis (Fig. 7). The TSC correlation value after a 1-h lag is still fairly significant at 0.59, whereas the traditional Barnes value has dropped to 0.26. It is interesting to observe that the correlation reaches a secondary maximum at 90–110 min, as a mesoscale feature that is lost between two stations by the traditional Barnes scheme reappears at the downstream station. These calculations emphasize the increase in wave resolution and coherence realized by including TSC in the objective analysis.

Dominant features in the analyzed fields are realistically coherent in space and time and are more indicative of the true propagation and shape of the observed features.

#### 4. Events examined from automated analyses

We demonstrate the usefulness of the automated mesoanalysis system through the investigation of two of the four events that have been processed since the system was activated in February 1999. The first case (11–12 March 2000) is of a gravity wave train that originated in western Kentucky and propagated northeastward through Ohio in conjunction with banded precipitation. The second case (12–14 March 1999) concerns a mesohigh/wake-low couplet associated with a mesoscale convective system that propagated from eastern Mississippi into western Georgia. Pressure falls of 5.5 hPa in 15 min and winds gusting in excess of 40 kt were reported with passage of the wake-low in Alabama. In both of these cases, relationships between the surface fields produced from the ASOS data and the radar imagery are discussed.

##### *a. Event 1 (11 March 2000)*

The synoptic situation was first examined for evidence of gravity wave potential from the 80-km Eta numerical model forecast fields. The 6-h Eta model forecast valid for 1800 UTC 11 March displays a surface low-pressure center in southern Kentucky and a deep 300-hPa trough over the Mississippi Valley region (Fig. 8). According to the UK87 conceptual model, gravity wave development would be most likely in the region of separation between the geostrophic wind maximum over Mississippi and the jet streak displaced to its northeast over the Great Lakes. This region is near the inflection axis in the 300-hPa height field, and the maximum in the residual of the nonlinear balance

equation is nearby (Fig. 9b). Gravity-inertia waves *generated* in this region would be *maintained* for a considerable distance downstream because of the favorable ducting environment over the Great Lakes, especially in Ohio (Fig. 9a).

Given the reasonably good potential for gravity wave development, the automated analysis system was activated in this region beginning at 1500 UTC 11 March 2000. Mesoanalyses conducted at 15-min intervals from then until 2100 UTC captured the wave evolution and movement. Hourly positions of the individual ridges and troughs in the wave train for 1830, 1930, and 2030 UTC are displayed alongside the composite radar imagery in Fig. 10. Multiple propagating wave-like features were evident during this time, but the most prominent of these was a wave train consisting of three trough-ridge pairs (T1/R1, etc.).

The wave train at 1830 UTC (Fig. 10a) consists of strengthening pressure perturbations R1, R2, and T1 in extreme southeastern Indiana. During the next 30 min, the pressure perturbations become organized into a succession of three trough-ridge pairs. Examination of the succession of radar images reveals a concurrent strengthening and organization of a single convective band of precipitation initially extending from southeastern Indiana to central Kentucky (Fig. 10d). This band appears better developed by 1930 UTC (Fig. 10e), when the strongest and most bowed-out part of the main precipitation band is located just ahead of ridge axis R1. The wave train reaches peak intensity by 2030 UTC as deduced from the  $p'$  fields. The northern portion of the main precipitation band continues to lie just ahead of wave ridge R1. Behind this band is a region of weaker reflectivity with sporadic breaks in precipitation associated with intensifying trough T2.

A small secondary precipitation band begins to appear in northern Kentucky at 2030

UTC (Fig. 10f) and strengthens thereafter (not shown). This band directly corresponds with ridge R2 in the wave train. A third wave crest (R3) is barely defined in the pressure perturbation field, and no precipitation band ever appears in conjunction with this weak feature. A strong wave trough (T3) propagates into southeastern Indiana after 2030 UTC. The strength of this trough and the weakness of wave ridge R3 appears to have prevented the development of further precipitation bands, as is evident by a broad clear zone behind the second precipitation band. Note also the development of an echo minimum or echo-free patch in central Kentucky at 1830 UTC, eastern Kentucky at 1930 UTC and western West Virginia at 2030 UTC. This developing patch existed just ahead of intensifying trough T2 at all times.

In summary, precipitation bands generally appeared a quarter-wavelength ahead of wave ridges and echo minima were found just ahead of wave troughs. These relationships are consistent with typical gravity wave behavior (Eom 1975; Koch et al. 1988). Further confirmation that these pressure perturbations (Figs. 11a–c) are actual manifestations of gravity waves is found in the pattern of the wave-normal wind perturbations (Figs. 11d–f). These anomalies appear very coherent, and throughout the duration of the wave event, the strongest  $u^*$  perturbations are highly correlated with the  $p'$  perturbations. The  $p'-u^*$  cross covariance fields reveal high positive values for each ridge and trough within the wave train at each time (Figs. 11g–i). These high correlations provide strong evidence that a gravity wave train is the dominant signal in the domain according to the wave impedance relation (Gossard and Hooke 1975; KOH97).

A non-filtered, non-perturbation mesoanalysis of the 5-min altimeter pressure and wind data could also be used to discern the gravity waves as a series of “wiggles” or anomalies in the isobars on the north-to-

northwest side of the surface cyclone (Fig. 12). The wind field also reflects the passage of the wave through distinct wind shifts along the nodal lines between each wave trough and ridge. Winds are directed from the northeast toward the wave troughs (negative  $u^*$ ) and vice versa for wave ridges, though this behavior is much more apparent in the  $u^*$  plots. This observation is consistent with the conceptual model for gravity waves. The evidence presented here suggests that the series of propagating pressure perturbations is a mesoscale gravity wave train, and that the wave packet had a strong influence upon the surface winds and precipitation fields.

#### *b. Event 2 (12–14 March 1999)*

Neither the upper-level synoptic flow nor the unbalanced flow indicators diagnosed from Eta model forecast fields suggested the potential for gravity wave formation according to the UK87 conceptual model in the 12–14 March 1999 case. However, a band of strong convection developed over Alabama and Georgia. Because the entire weather system had been tracked by the automated system ever since it originated in Oklahoma on 12 March (discussed in section 5), it was decided to continue the mesoanalyses throughout the entire weather event to the East Coast. System advection vectors were determined from the vector mean winds in the 700–400 hPa conditionally unstable layer as deduced from the conventional radiosonde data. The sensitivity tests discussed earlier, which were performed upon this case, demonstrated that the mesoanalysis results were not sensitive to moderately large deviations in the advection vector directions. The following discussion emphasizes a complex ensemble of mesoscale pressure features accompanying a broad mesoscale convective system (MCS) that propagated eastward from central Alabama at 0000 UTC to central Georgia by 0600 UTC.

Before proceeding with the analysis of this case, it is beneficial to briefly review current understanding of surface mesolows and mesohighs associated with MCSs. Johnson (2001) recently reviewed the pioneering work of Tetsuya Fujita and subsequent research on surface pressure fields that attend deep, moist convection. Essentially three types of mesoscale pressure features occur at the surface: the mesohigh, the wake-low, and the presquall mesolow (Fig. 13). Fujita showed in a series of early papers [as reviewed in Fujita (1963)] that the primary contributor to the mesohigh is evaporation of rain that falls below cloud base, and that the wake-low does not develop until after the mesohigh reaches its maximum intensity. Williams (1963) proved that subsidence warming could explain the observed pressure deficit in the wake-low. Yet, it was not until the discovery of the leading-convective-line/trailing-stratiform structure, and the associated front-to-rear and rear-to-front circulations (Zipser 1977; Smull and Houze 1985, 1987a,b) that the wake-low could be fully understood. Johnson and Hamilton (1988) succinctly summarized the mass of evidence showing that the wake-low is a hydrostatic consequence of the rapid dry descent of the rear-to-front inflow jet, which is maximized at the back edge of the precipitation area. In fact, the most intense pressure gradient often appears to lie precisely at the back edge of the stratiform precipitation area. Vescio and Johnson (1992) further showed that the maximum divergence is found behind the mesohigh, the maximum easterly flow precedes the wake-low, and the maximum westerly flow precedes the mesohigh. Finally, the presquall mesolow was first documented by Hoxit et al. (1976), further observed in many subsequent studies, and later modeled by Fritsch and Chappell (1980). These studies demonstrated that this mesolow is caused by compensatory subsidence warming in the middle-upper troposphere ahead of squall lines.

Hourly displays of  $p'$  fields for 14 March 1999 (Fig. 14) reveal the evolution and movement of mesohighs, wake-lows, and presquall mesolows relative to the MCS. These mesoanalyses show that the convectively induced pressure field is comprised of multiple features that form, mature, propagate, and dissipate throughout the convective system. An examination of the interaction between the pressure perturbations and the convection shows that the pressure perturbation signatures in this event are manifestations of the convection itself. For example, a mesoscale pressure ridge composed of two mesohighs (H1 and H2) remains coupled with the center of the convective region of enhanced radar reflectivity throughout the 4-h period. The mesohigh and convective region achieve maximum strength together by 0230 UTC, after which the mesohigh begins to show a decrease in amplitude and the convective system begins to become disorganized and weaken. This behavior is consistent with the knowledge that mesohighs owe their existence primarily to evaporation of precipitation.

Three trailing wake-lows (WL1, WL2, WL3) are also revealed in the  $p'$  plots. The mesoanalyses shown here capture WL1 during its dissipation stage, in concert with the flattening out and disintegration of associated mesohigh H1 and weakening of nearby radar reflectivity fields. In a similar manner, WL2 remains attached to the backside of associated mesohigh H2 and the radar reflectivity field. The merger of new wake-low WL3 with WL2 at 0330 UTC further strengthens WL2. This close association between individual mesohighs and wake-lows may be attributed to the fact that wake-lows are associated with trailing stratiform precipitation regions, which are in turn maintained by the front-to-rear flow above surface cool pools and their associated mesohigh pressure systems (Johnson 2001).

In the present case, a large fraction of the MCS radar pattern is composed of stratiform precipitation. The merger of WL2 and WL3 produces a strong wake low that reaches peak intensity at approximately 0400 UTC in northeastern Alabama. As the wake-low passed over Anniston, Alabama, the station experienced a pressure plunge of 5.5 hPa in 15 min and resultant *easterly* wind gusts > 40 kt. This wake-low began to decrease in intensity and size afterward in association with the deterioration in the organization and strength of the overall MCS.

The mesoanalyses reveal that the back edge of H2 develops somewhat of a bowed appearance after 0030 UTC simultaneously with the rapid development of WL2 and WL3. These observations are suggestive of a rear-inflow jet forcing its way into the convective region. Although this cannot be proven from the given data, it is consistent with the understanding that a rapidly descending rear-inflow jet can create a local “clear zone” in the precipitation and local pressure falls due to subsidence-induced warming near the surface (Fig. 13a). In fact, the northwestern portion of the MCS appears to dissolve the fastest.

Another feature found in this MCS, though less intense than the wake-low, is the presquall mesolow. At first glance, this weak feature could be easily overlooked, yet the presquall mesolow in this case remains a prominent signature for the duration of the event. The initial presquall mesolow (PSL1) is observed at the first available time (0030 UTC). PSL1 slowly progresses to the northeast (downshear) of the main mesohigh H2. A second presquall mesolow (PSL2) appears by 0330 UTC and exhibits a similar morphology to that of PSL1 (not shown). Johnson and Hamilton (1988) found this kind of system-relative movement to be characteristic of presquall mesolows.

Surface winds were examined for signatures that could be related to the mesohigh and wake-low phenomena, and

compared to both the Fujita (1955, 1963) thunderstorm model and the Johnson and Hamilton (1988) mesoscale convection model. Surface mesoanalyses of the altimeter pressure and winds and subjectively analyzed fronts are displayed in Fig. 15. Examination of these analyses shows a distinct maximum in the easterly winds within the zone of strong pressure gradient field between mesohigh H2 and wake-low WL2/WL3 in central and eastern Alabama. This relationship is consistent with the Johnson and Hamilton (1988) model for a squall line convective system. Vescio and Johnson’s (1992) refined conceptual model more adequately explains the intricate pressure and wind patterns within the mesohigh/wake-low couplet, yet, with the coarse ASOS station spacing, the mesoanalysis system cannot fully resolve the finest scale features. Despite the limitation of fine-scale resolution within the ASOS network, the analyzed pressure-wind relationship is not consistent with a gravity wave interpretation, in which the strongest easterly winds would occur in the center of the mesolow.

## 5. Discussion

Upon recognition of a favorable environment for the development of potentially threatening mesoscale phenomena, the automated ASOS mesoanalysis system that has been developed and discussed herein may be activated. Because of restrictions imposed by the modem-based data access system and the policy established for data access for this project, only ~75 stations could be dialed up in each of three access windows daily. This necessitated the creation of analysis subregions and the retrieval of 5-min data for ~10 h periods of time. Consequently, this system produced analyses that were ~4.5 h behind real time.

The first step in the mesoanalysis procedure was to parse the ASOS data to obtain relevant meteorological parameters.

These data were then subjected to various quality control procedures to eliminate erroneous data. Next, time series of altimeter pressure and wind components for each station were bandpass-filtered in order to isolate mesoscale perturbations with periods between 30 min and 4 h. These filtered data were then objectively analyzed using a time-to-space conversion (TSC) adaptation of the Barnes objective analysis scheme. Results of sensitivity tests suggested that the best mesoanalyses are obtained by using multiple TSC advection vectors, and performing TSC over an interval of  $\tau = 50$  min. Sensitivity tests also reveal the superior analysis capability of TSC over the traditional Barnes scheme, provided that one can specify a set of advection vectors that are representative of the motion of the mesoscale system(s).

The development of this automated mesoanalysis system was originally intended for the detection of mesoscale gravity waves in pseudo-real-time in order to make the nowcasting of such features a possibility in an operational forecasting environment. Gravity waves and other mesoscale features have remained primarily a research concern, with little hope for their operational detection and analysis. We have taken what has traditionally been a multimonth-long process of analyzing a gravity wave event (Uccellini 1975; Bosart and Sanders 1986; Koch and Golus 1988; Koch et al. 1998) and made it possible to complete very detailed mesoanalyses in a matter of only a few hours behind real time. This is a huge improvement that is only limited by the data transfer system (dial-up modem calling  $\sim 75$  stations at 1–2 minutes per station), data filtering constraints, and the computer processing time (30 min). If ASOS data could be made available over the Internet and a spatial bandpass filter were to replace the temporal bandpass filter used herein, the analysis system could be run continuously while very closely approaching real time.

It has been shown that this mesoanalysis system is also capable of revealing other phenomena that exhibit wavelengths and time scales similar to mesoscale gravity waves. Surface frontal deformation zones, gust fronts, and convective phenomena can also be captured by this automated mesoanalysis system. Depending upon the phenomenon of interest, a specific advection vector should be manually entered into the scheme to reflect the given system motion (e.g., cold frontal motion vector). In more complex situations that involve differing motions of frontal systems, gravity waves, mesoconvective systems, gust fronts, sea breeze convergence zones, terrain features, and so forth, it is more difficult to determine representative advection vectors. However, it would not be difficult to create a system using the graphical user interface for the Local Analysis and Prediction System (LAPS; Albers et al. 1996) on the Advanced Weather Interactive Processing System (AWIPS) to enable a forecaster to interactively determine representative advection vectors on a map or satellite image. This would be restricted to only those situations where mesoanalyses are needed to support the short-range forecast process.

An even brighter future of performing extremely detailed mesoanalyses in real time lies in the expected increase in the density of the surface observing network. The Oklahoma Mesonet and similar state mesonetworks either in place or under development can produce incredible detail in the analysis fields. Furthermore, because of the use of bandpass filtering, absolute inaccuracies in such non-operational datasets are not a problem. The ASOS network for the Oklahoma region and the Oklahoma Mesonet station network may be compared in [Fig. 16](#). Average station spacing for the Oklahoma Mesonet is  $\sim 35$  km, compared to  $\sim 90$  km for the depicted ASOS network. Analyzed pressure perturbation fields are compared for three specific times in [Fig. 17](#). Note the

remarkable detail provided by the Oklahoma Mesonet analysis in comparison to the much coarser resolution of the ASOS mesoanalysis, even when using TSC with the 5-min ASOS data. Structure and amplitude of all pressure features are greatly enhanced by the use of such detailed mesoscale data. This comparison reveals the great potential for conducting very detailed mesoanalyses with enhanced spatial resolution provided by the inclusion of additional mesonet data with the ASOS network. Such data could be analyzed and displayed on AWIPS through the LAPS system, particularly if the TSC analysis methodology applied to the 5-min data is adapted to LAPS.

This study has shown that the high temporal information contained in the ASOS data (and surface mesonetworks in the future) can be utilized to recover the full amplitude, structure, and coherence of mesoscale features. Current reliance upon hourly data by the NWS will not suffice for such purposes. Detailed real-time surface mesoanalyses will be an invaluable asset to

operational forecasters and researchers alike, and these analyses shall certainly help to improve operational mesoscale nowcasting.

*Acknowledgments.* We are indebted to the National Weather Service for allowing us access by modem to the high temporal resolution ASOS data comprising the foundation of this work. The authors would also like to express their appreciation to Gary Lackmann, Yuh-Lang Lin, and Al Riordan of North Carolina State University and to John McGinley and Nita Fullerton of NOAA Forecast Systems Laboratory for their helpful comments on this manuscript. The National Science Foundation supported this research under grant ATM-9700626. This research was also funded in part from a subaward under a cooperative agreement between the National Oceanic and Atmospheric Administration (NOAA) and the University Corporation for Atmospheric Research (UCAR) pursuant to UCAR Subaward No. S96-75675 pursuant to NOAA Award No. NA57GP0567.

---

## References

- Albers, S., J. McGinley, D. Birkenheuer, and J. Smart, 1996: The Local Analysis and Prediction System (LAPS): Analyses of clouds, precipitation, and temperature. *Wea. Forecasting*, **11**, 273–287.
- Barnes, S.L., 1964: A technique for maximizing details in numerical weather map analysis. *J. Appl. Meteor.*, **3**, 396–409.
- \_\_\_\_\_, 1973: Mesoscale objective analysis using weighted time-series observations. NOAA Tech. Memo ERL NSSL-62, National Severe Storms Laboratory, 60 pp. [NTIS COM-73-10781.] [Available from NOAA National Severe Storms Laboratory, 1313 Halley Circle, Norman, OK 73019.]
- Bosart, L.F., and F. Sanders, 1986: Mesoscale structure in the megalopolitan snowstorm of 11-12 February 1983. Part III: A large-amplitude gravity wave. *J. Atmos. Sci.*, **43**, 924–939.
- Eom, J.K., 1975: Analysis of the internal gravity wave occurrence of 19 April 1970 in the Midwest. *Mon. Wea. Rev.*, **103**, 217–226.

- Friday, E. W. Jr., 1993: Associated restructuring of the National Weather Service: An overview. *Bull. Amer. Meteor. Soc.*, **75**, 43–48.
- Fritsch, J. M., and C. F. Chappell, 1980: Numerical prediction of convectively driven mesoscale pressure systems. Part I: Convective parameterization. *J. Atmos. Sci.*, **37**, 1722 – 1733.
- Fujita, T.T., 1955: Results of detailed synoptic studies of squall lines. *Tellus*, **4**, 405–436.
- \_\_\_\_\_, 1963: Analytical mesometeorology: A review. *Severe Local Storms Meteor. Monogr.*, No. 27, Amer. Meteor. Soc., 77–125.
- Gossard, E.E., and W.H. Hooke, 1975: *Waves in the Atmosphere*. Elsevier, 456 pp.
- Hoxit, L. R., C. F. Chappell, and J. M. Fritsch, 1976: Formation of mesolows or pressure troughs in advance of cumulonimbus clouds. *Mon. Wea. Rev.*, **104**, 1419–1428.
- Johnson, R.H., 2001: Surface mesohighs and mesolows. *Bull. Amer. Meteor. Soc.*, **82**, 13–31.
- \_\_\_\_\_, and P.J. Hamilton, 1988: The relationship of surface pressure features to the precipitation and airflow structure of an intense midlatitude squall line. *Mon. Wea. Rev.*, **116**, 1444–1472.
- Koch, S. E., and J. McCarthy, 1982: The evolution of an Oklahoma dryline. Part II: Boundary-layer forcing of mesoconvective systems. *J. Atmos. Sci.*, **39**, 237–257.
- \_\_\_\_\_, and R.E. Golus, 1988: A mesoscale gravity wave event observed during CCOPE. Part I: Multiscale statistical analysis of wave characteristics. *Mon Wea. Rev.*, **116**, 2527–2544.
- \_\_\_\_\_, and C. O'Handley, 1997: Operational forecasting and detection of mesoscale gravity waves. *Wea. Forecasting*, **12**, 253–281.
- \_\_\_\_\_, and L.M. Siedlarz, 1999: Mesoscale gravity waves and their environment in the central United States during STORM-FEST. *Mon. Wea. Rev.*, **127**, 2854–2879.
- \_\_\_\_\_, M. desJardins, and P.J. Kocin, 1983: An interactive Barnes objective map analysis scheme for use with satellite and conventional data. *J. Climate Appl. Meteor.*, **22**, 1487–1503
- \_\_\_\_\_, R.E. Golus, and P.B. Dorian, 1988: A mesoscale gravity wave event observed during CCOPE. Part II: Interactions between mesoscale convective systems and the antecedent waves. *Mon. Wea. Rev.*, **116**, 2545–2569.
- \_\_\_\_\_, D. Hamilton, D. Kramer, and A. Langmaid, 1998: Mesoscale dynamics in the Palm Sunday tornado outbreak. *Mon. Wea. Rev.*, **126**, 2031–2060.
- Koppel, L.L., L.F. Bosart, and D. Keyser, 2000: A 25-yr climatology of large-amplitude hourly surface pressure changes over the conterminous United States. *Mon. Wea. Rev.*, **128**, 51–68.

- Lanczos, C., 1956: *Applied Analysis*. Prentice-Hall, 539 pp.
- Lindzen, R.S., and K.K. Tung, 1976: Banded convective activity and ducted gravity waves. *Mon. Wea. Rev.*, **104**, 1602–1617.
- Smull, B.F., and R.A. Houze, Jr., 1985: A midlatitude squall line with a trailing region of stratiform rain: Radar and satellite observations. *Mon. Wea. Rev.*, **113**, 117–133.
- \_\_\_\_\_, and \_\_\_\_\_, 1987a: Dual-Doppler radar analysis of a mid-latitude squall line with a trailing region of stratiform rain. *J. Atmos. Sci.*, **44**, 2128–2148.
- \_\_\_\_\_, and \_\_\_\_\_, 1987b: Rear inflow in squall lines with trailing stratiform precipitation. *Mon. Wea. Rev.*, **115**, 2869–2889.
- Uccellini, L.W., 1975: A case study of apparent gravity wave initiation of severe convective storms. *Mon. Wea. Rev.*, **103**, 497–513.
- \_\_\_\_\_, and S.E. Koch, 1987: The synoptic setting and possible energy sources for mesoscale wave disturbances. *Mon. Wea. Rev.*, **115**, 721–729.
- Vescio, M. J., and R. H. Johnson, 1992: The surface-wind response to transient mesoscale pressure fields associated with squall lines. *Mon. Wea. Rev.*, **120**, 1837-1850.
- Williams, D. T., 1963: The thunderstorm wake of May 4, 1961. Nat. Severe Storms Project Rep. 18, U.S. Dept. of Commerce, Washington DC, 23 pp. [NTIS PB-168223.]
- Zhang, F., and S.E. Koch, 2000: A survey of unbalanced flow diagnostics and their application. *Advances in Atmospheric Sciences*, **17**, 165–183.
- Zipser, E. J., 1977: Mesoscale and convective-scale downdrafts as distinct components of squall-line circulation. *Mon. Wea. Rev.*, **105**, 1568–1589.

## Figure Legends

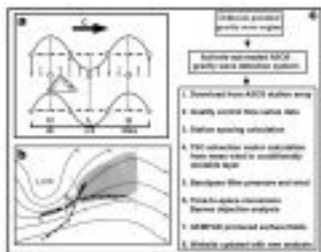


FIG. 1. (a) Eom (1975) conceptual model of pressure and wind patterns (horizontal and vertical vectors) associated with trapped (non-tilted) gravity waves, and the relationship of these patterns to the wave-induced clouds for a gravity wave with a 160-km wavelength propagating to the right at speed  $C$ . (b) schematic model of UK87 delineating the region of greatest potential for gravity wave occurrence (shaded) downstream of the wave generation region, which develops as an upper-level jet streak ( $V$ ) approaches the axis of inflection (dashed line) in the height field (solid lines). (c) flowchart of the operational procedure for the prediction and automated detection of mesoscale gravity waves.

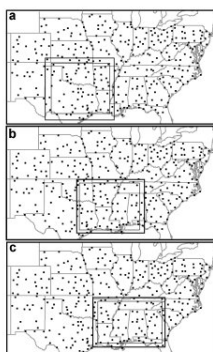


FIG. 2. Three of the nine ASOS sub-regions in which mesoanalyses were performed. Dots are ASOS stations, the outer box is the data download region, and the inner box is the objective analysis region.

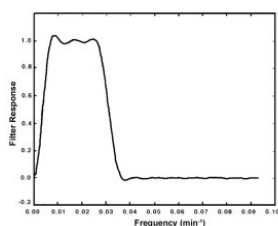


FIG. 3. The bandpass filter in this study uses 49 weights and has peak response for frequencies of 0.0037 - 0.0313  $\text{min}^{-1}$ , corresponding to waves with periods of 32 - 270 min.

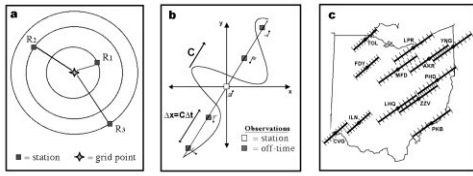


FIG. 4. (a) The time-to-space conversion (TSC) Barnes scheme makes use of the exponential spatial weighting function  $W = \exp(-R^2 / K)$ , where  $R$  is the distance from each station within a certain radius of influence to the grid point and  $K$  is a constant, and (b) an advection vector  $C$  to fill in gaps between available reporting stations by converting off-time data into (c) spatial data (tics) along the direction of the advection vector centered about each available station. The off-time data are weighted by their temporal distance from the on-time observation (the analysis time) using an inverse Gaussian function similar in form to that of the spatial weighting function.

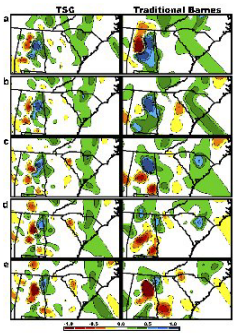


FIG. 5. Pressure perturbation mesoanalyses (hPa) at (a) 0245, (b) 0300, (c) 0315, (d) 0330, and (e) 0345 UTC 14 March 1999. Plots provide a comparison between analyses using (left) the TSC Barnes scheme with  $\tau = 50$  min and four advection vectors and (right) the traditional Barnes scheme.

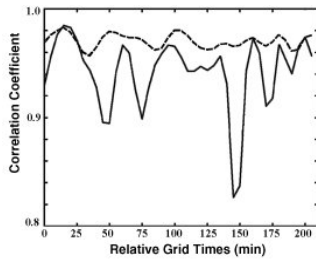


FIG. 6. Domain correlation values for successive grids of pressure perturbations over the period 0100 to 0430 UTC 14 March 1999 for the traditional Barnes scheme (solid line) and the TSC Barnes using four advection vectors (dotted line). Note the consistently high correlation values for the TSC case.

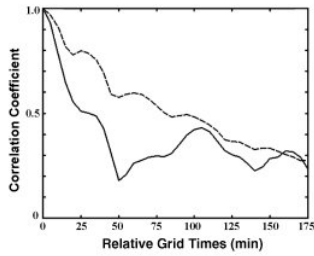


FIG. 7. Time-lagged correlation values for a 3-h data sample from 0100–0400 UTC 14 March 1999. Solid line is for the traditional Barnes analysis. Dashed line is the correlation coefficient curve for the TSC Barnes analysis.

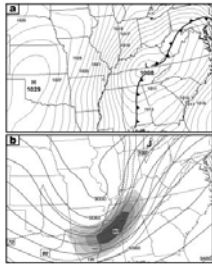


FIG. 8. Six-hour Eta model forecast fields valid for 1800 UTC 11 March 2000 of (a) mean sea level pressure and (b) 300-mb heights (solid), isotachs of wind speed exceeding  $70 \text{ m s}^{-1}$  (dashed) and isotachs of the geostrophic wind exceeding  $130 \text{ m s}^{-1}$  (shaded). Isobars are at 1 hPa intervals, isotachs are at  $10 \text{ m s}^{-1}$  intervals, and geopotential height contours are every 60 gpm.

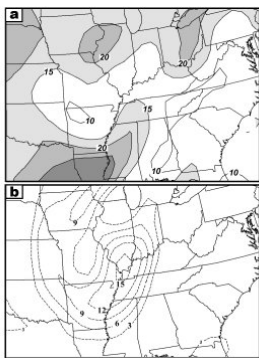


FIG. 9. Diagnostics from 6-h Eta model forecast valid at 1800 UTC 11 March 2000: (a) Duct factor field ( $^{\circ}\text{C}$ ) and (b) residual of nonlinear balance equation ( $10^{-8} \text{ sec}^{-2}$ , dashed lines).

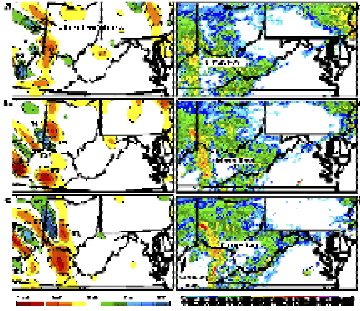


FIG. 10. Comparisons between (a–c) pressure perturbation mesoanalyses (hPa), and (d–f) composite radar reflectivity fields (dBZ) at 1830, 1930, and 2030 UTC 11 March 2000, respectively. R1 refers to ridge #1, T1 refers to trough #1, and so forth.

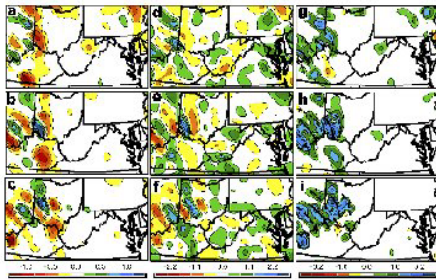


FIG. 11. Perturbation fields at 1900, 2000, and 2100 UTC 11 March 2000: (a–c) pressure perturbations (hPa), (d–f) wave-normal wind perturbations ( $\text{m s}^{-1}$ ), and (g–i) pressure-wind cross-covariance fields with overlaid ridge (solid) and trough (dashed) wave positions.

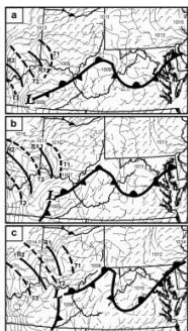


FIG. 12. Surface mesoanalysis of altimeter pressure (solid lines), wind barbs (kt), wave troughs and ridges (dashed and solid bold lines) at (a) 1900, (b) 2000, and (c) 2100 UTC 11 March 2000.

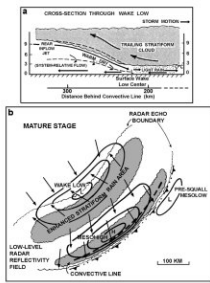


FIG. 13. (a) Schematic cross section through the wake low at the trailing edge of a mature squall line and (b) surface pressure and wind fields and precipitation distribution (shading). Winds in (a) are system-relative, with the dashed line representing the zero relative wind. Arrows are streamlines in (a) and the observed wind in (b). Note the different horizontal scales used in the two schemata (Johnson and Hamilton 1988).

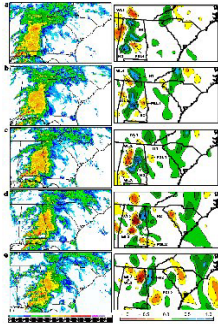


FIG. 14. NOWRAD composite radar reflectivity (dBZ) and pressure perturbation mesoanalyses (hPa) at (a) 0030, (b) 0130, (c) 0230, (d) 0330, and (e) 0430 UTC 14 March 1999. WL refers to the wake-low, H refers to the mesohigh, and PS refers to the pre-squall mesolow.

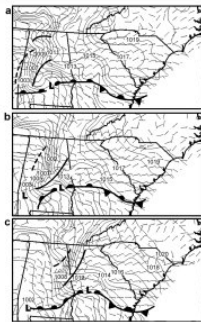


FIG. 15. Surface mesoanalyses of altimeter pressure (1 hPa isobars), wind barbs (kt), mesohighs and wake-lows (solid and dashed bold lines, respectively), and frontal features at (a) 0030, (b) 0230, and (c) 0430 UTC 14 March 1999.

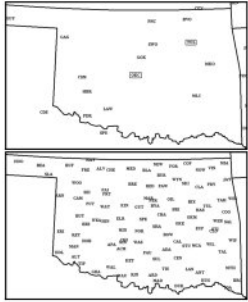


FIG. 16. Stations available for analysis on 12 March 1999 within (a) the ASOS network and (b) the Oklahoma Mesonet. Boxed stations were not available for the analyses shown in Fig. 17 a–c.

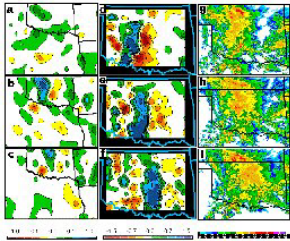


FIG. 17. (a–c) Mesoanalyses of pressure perturbations (hPa) from ASOS network shown in Fig. 16a at 1600, 1700, and 1800 UTC 12 March 1999, respectively. (d–f) mesoanalyses of pressure perturbations analyzed from the Oklahoma Mesonet data (Fig. 16b) for the same times as in (a–c). (g–i) composite radar images for the same times.